HHS Public Access

Author manuscript

Appl Magn Reson. Author manuscript; available in PMC 2023 May 01.

Published in final edited form as:

Appl Magn Reson. 2022 May ; 53(3-5): 699–715. doi:10.1007/s00723-021-01390-7.

Theory and Least Squares Fitting of CW ESR Saturation Spectra Using the MOMD Model

Pranav Gupta[1], **Boris Dzikovski**[1,2], **Jack H. Freed**[1]

[1]National Biomedical Center for Advanced ESR Technology and Department of Chemistry and Chemical Biology, Cornell University, Ithaca, NY 14853, USA

[2]Bruker BioSpin Corp, 15 Fortune Drive, Billerica, MA 01821, USA

Abstract

CW saturation experiments are widely used in ESR studies of relaxation processes in proteins and lipids. We develop the theory of saturation in ESR spectra in terms of its close relation with that of 2D-ELDOR. Our treatment of saturation is then based on the microscopic order macroscopic disorder (MOMD) model and can be used to fit the full CW saturation spectrum, rather than fitting just the peak–peak amplitude as a function of microwave field B_1 as is commonly done. This requires fewer experiments to yield effects on T_1, as well as provides a more extensive dynamic structural picture, for example, for scanning experiments on different protein sites. The code is released as a publicly available software package in Python that can be used to fit CW saturation spectra from biological samples of interest.

1 Introduction

Spin label ESR is a useful approach for the study of biological systems such as membranes and proteins. Especially important has been pulse dipolar ESR to determine protein structure [1, 2]. This technique is performed at low temperatures in the frozen state. But ESR can very effectively be used for studies at ambient temperatures both in structural studies and for dynamics [3, 4]. The dynamic studies have required sophisticated theoretical methods for their interpretation especially for ordered systems like membranes and slowly tumbling proteins in solution based on the stochastic Liouville equation (SLE). The associated experimental methods are typically either based on CW ESR spectra that are unsaturated or else pulse methods such as 2D-ESR. However, CW saturation has been used in the past to study relaxation processes and is currently used to determine protein secondary structure at ambient temperatures [5, 6]. It is based on how O_2 or Ni complexes affect the T_1's of nitroxide labels at the different protein amino acid positions employing a simple heuristic formula and method. However, the theoretical methods needed for more rigorous analysis of the CW saturation spectra are implicitly contained in existing software for unsaturated CW and pulse experiments such as that employing the MOMD (microscopic order and macroscopic disorder) model. This model [7] has been shown to be useful for motions

✉Jack H. Freed, jhf3@cornell.edu.

in membranes as well as local motions in proteins which are very slowly tumbling in solution. It is the purpose of this paper to develop the analysis and software that already exists for unsaturated CW and pulsed ESR into an effective program for CW saturation experiments. This will provide the dual advantages of reducing the number of saturation experiments required to obtain the T_1 enhancements and at the same time provide more detailed information on the dynamic structure of the different protein sites.

Early theoretical descriptions of saturation in CW ESR spectroscopies were given by Stephen and Fraenkel [8] and by Freed [9] addressing the motional narrowing region for free radicals. The first description of saturation for spectra in the slow motional region was presented by Goldman et al. [10] utilizing a simple Brownian-type description of the dynamics. Since then the more sophisticated MOMD model [7, 11] was found to adequately describe the dynamics, and software was developed for this purpose. The emergence of the 2D-ESR technique of 2D-ELDOR (two dimensional electron–electron double resonance) led to useful software [12, 13] which benefited from the fact that during the longer evolution times in the experiment, when the molecular motions develop, there is no microwave radiation present, but during the very short periods of intense pulses they dominate. But for CW, the microwave radiation is constantly present, so the molecular dynamics and the effects of the radiation must be considered simultaneously [10]. Yet the elements of the SLE contained in the theory for 2D-ELDOR are sufficient for the CW case with just rearrangement of the appropriate components of the SLE needed. This is the approach taken in the present paper. We then demonstrate its utility by comparison with experiments on a spin labeled lipid contained in lipid vesicles where a MOMD approach is needed.

2 Theory of ESR Saturation Spectra

The evolution of the orientation-dependent density matrix $\rho(\Omega, t)$ is given by the stochastic Liouville equation (SLE): [12, 14]

$$\frac{\partial \rho(\Omega,t)}{\partial t} = -\imath[\mathscr{H}, \rho(\Omega,t)] - \Gamma_{\Omega}\big(\rho(\Omega,t) - \rho_{eq}\big) \tag{1}$$

Here Ω denotes the orientation of the spin label and $\mathscr{L}$ denotes the Liouville operator. Equation (1) can be rewritten as:

$$\frac{\partial \rho(\Omega,t)}{\partial t} = -\imath\mathscr{H}^{\times}\rho(\Omega,t) - \Gamma_{\Omega}\rho(\Omega,t) + \Gamma_{\Omega}\rho_{eq}(\Omega) = -\mathscr{L}\rho(\Omega,t) + \Gamma_{\Omega}\rho_{eq}(\Omega), \tag{2}$$

where $\mathscr{L}$ is the stochastic Liouville operator. For the case of a saturating microwave field, the SLE can be written as: [10, 15–18]

$$\frac{\mathrm{d}}{\mathrm{d}t}\begin{bmatrix}\mathbf{Z}(t)\\ \mathbf{Z}^*(t)\\ \chi(t)\end{bmatrix} = -\begin{bmatrix}\mathscr{L}_{+1} - \imath\omega\mathbb{I} & 0 & \imath\mathscr{D}\\ 0 & \mathscr{L}_{-1} + \imath\omega\mathbb{I} & -\imath\mathscr{D}\\ \imath\mathscr{D}^T & -\imath\mathscr{D}^T & \mathscr{L}_0\end{bmatrix}\begin{bmatrix}\mathbf{Z}(t)\\ \mathbf{Z}^*(t)\\ \chi(t)\end{bmatrix} + \begin{bmatrix}\imath\mathbf{Q}\\ -\imath\mathbf{Q}\\ 0\end{bmatrix} \tag{3}$$

Here $\mathbf{Z}(t) = \mathbf{Z}'(t) + \imath\mathbf{Z}''(t)$ is the first harmonic of the $p^S = 1$ coherence components of the density matrix $\rho(\Omega, t)$, written in a Liouville space format. Given the Hermitian (self-adjoint)

nature of $\rho(\Omega, t)$, the corresponding components in the $p^S = -1$ coherence are given as $\mathbf{Z}^*(t) = \mathbf{Z}'(t) - \imath\mathbf{Z}''(t)$, and ω denotes the frequency offset from resonance.

$\chi(t)$ denotes the deviation of the $p^S = 0$ coherence components of $\rho(\Omega, t)$ from the equilibrium density matrix $\rho_{eq}(\Omega)$.

$\mathscr{L}_0$, $\mathscr{L}_{+1}$ and $\mathscr{L}_{-1}$ denote the stochastic Liouville matrices corresponding to the electronic coherence orders $p^S = 0, +1, -1$ respectively.

$\mathscr{D}$ denotes the transition-moment matrix that connects the off-diagonal matrix elements of $\rho(\Omega, t)$ to its diagonal elements. $\mathscr{D}$ is proportional to the applied saturating field B_1. The derivation of $\mathscr{D}$ from first principles is described later in the text.

Note that $\mathscr{L}_0$, $\mathscr{L}_{+1}$, $\mathscr{L}_{-1}$, as well as the 3 × 3 block matrix in Eq. (3), are all complex symmetric.

Q is closely related to the off-diagonal space starting vector [12] used in the analysis of pulsed 2D-ELDOR spectroscopy experiments. The non-zero elements of **Q** correspond to the allowed ESR transitions. The expression for **Q**, after neglecting constant factors, is:

$$\mathbf{Q} \propto B_1 |v_{+1}\rangle, \tag{4}$$

where v_{+1} denotes the starting vector in the off-diagonal space, i.e., $p^S = +1$ coherence order, as described elsewhere [12, 18].

The steady state solution of Eq. (3), obtained by putting the left hand side derivative term equal to 0, is given as:

$$0 = -\begin{bmatrix} \mathscr{L}_{+1} - \imath\omega[] & 0 & \imath\mathscr{D} \\ 0 & \mathscr{L}_{-1} + \imath\omega[] & -\imath\mathscr{D} \\ \imath\mathscr{D}^T & -\imath\mathscr{D}^T & \mathscr{L}_0 \end{bmatrix} \begin{bmatrix} \mathbf{Z}_{ss}(t) \\ \mathbf{Z}^*_{ss}(t) \\ \chi_{ss}(t) \end{bmatrix} + \begin{bmatrix} \imath\mathbf{Q} \\ -\imath\mathbf{Q} \\ 0 \end{bmatrix} \tag{5}$$

Rearranging Eq. (5), we get:

$$\begin{bmatrix} \mathbf{Z}_{ss}(t) \\ \mathbf{Z}^*_{ss}(t) \\ \chi_{ss}(t) \end{bmatrix} = \begin{bmatrix} \mathscr{L}_{+1} - \imath\omega[] & 0 & \imath\mathscr{D} \\ 0 & \mathscr{L}_{-1} + \imath\omega[] & -\imath\mathscr{D} \\ \imath\mathscr{D}^T & -\imath\mathscr{D}^T & \mathscr{L}_0 \end{bmatrix}^{-1} \begin{bmatrix} \imath\mathbf{Q} \\ -\imath\mathbf{Q} \\ 0 \end{bmatrix} \tag{6}$$

The CW absorbed power is proportional to the steady-state magnetization for the $p^S = -1$ coherence, which in turn is related to $\mathbf{Z}''(t)$:

$$P \propto \mathbf{Q}^T \mathbf{Z}''_{ss} = \mathrm{Im}\left(\mathbf{Q}^T \mathbf{Z}_{ss}\right) \tag{7}$$

Here Im(z) denotes the imaginary part of a complex z.

However, we know that

$$\mathbf{Q}^T\mathbf{Z}_{ss} = \begin{bmatrix}\mathbf{Q}^T & 0 & 0\end{bmatrix}\begin{bmatrix}\mathbf{Z}_{ss}(t)\\ \mathbf{Z}^*_{ss}(t)\\ \chi_{ss}(t)\end{bmatrix} = \begin{bmatrix}\mathbf{Q}\\ 0\\ 0\end{bmatrix}^T\begin{bmatrix}\mathscr{L}_{+1}-\iota\omega\mathbb{I} & 0 & \iota\mathscr{D}\\ 0 & \mathscr{L}_{-1}+\iota\omega\mathbb{I} & -\iota\mathscr{D}\\ \iota\mathscr{D}^T & -\iota\mathscr{D}^T & \mathscr{L}_0\end{bmatrix}^{-1}\begin{bmatrix}\iota\mathbf{Q}\\ -\iota\mathbf{Q}\\ 0\end{bmatrix} \tag{8}$$

Therefore, the absorbed power P is given as:

$$P \propto \mathrm{Im}\left(\mathbf{Q}^T\mathbf{Z}_{ss}\right) = \mathrm{Im}\left(\begin{bmatrix}\mathbf{Q}\\ 0\\ 0\end{bmatrix}^T\begin{bmatrix}\mathscr{L}_{+1}-\iota\omega\mathbb{I} & 0 & \iota\mathscr{D}\\ 0 & \mathscr{L}_{-1}+\iota\omega\mathbb{I} & -\iota\mathscr{D}\\ \iota\mathscr{D}^T & -\iota\mathscr{D}^T & \mathscr{L}_0\end{bmatrix}^{-1}\begin{bmatrix}\iota\mathbf{Q}\\ -\iota\mathbf{Q}\\ 0\end{bmatrix}\right) \tag{9}$$

In the non-saturating CW regime, which is in the limit of small B_1, the expression for the absorbed power turns out to be much simpler, as we can set the spin-transition matrices $\mathscr{D}$ to be 0, given that they are proportional to the applied microwave field B_1. By combining Eqs. (4) and (9), we get:

$$P \propto \mathrm{Im}\left(\begin{bmatrix}\mathbf{Q}\\ 0\\ 0\end{bmatrix}^T\begin{bmatrix}\mathscr{L}_{+1}-\iota\omega\mathbb{I} & 0 & 0\\ 0 & \mathscr{L}_{-1}+\iota\omega\mathbb{I} & 0\\ 0 & 0 & \mathscr{L}_0\end{bmatrix}^{-1}\begin{bmatrix}\iota\mathbf{Q}\\ -\iota\mathbf{Q}\\ 0\end{bmatrix}\right) \tag{10}$$

$$= \mathrm{Im}\left(\iota\mathbf{Q}^T\left(\mathscr{L}_{+1}-\iota\omega\mathbb{I}\right)^{-1}\mathbf{Q}\right) \tag{11}$$

$$= \mathrm{Re}\left(\mathbf{Q}^T\left(\mathscr{L}_{+1}-\iota\omega\mathbb{I}\right)^{-1}\mathbf{Q}\right) \tag{12}$$

$$= \mathrm{Re}\left(\mathbf{Q}^T\left(\mathscr{L}_{+1}-\iota\omega\mathbb{I}\right)^{-1}\mathbf{Q}\right) \tag{13}$$

$$= \left(\frac{B_1}{2}\right)^2\mathrm{Re}\left(v_{+1}^T\left(\mathscr{L}_{+1}-\iota\omega\mathbb{I}\right)^{-1}v_{+1}\right) \tag{14}$$

$$= \frac{B_1^2}{4}\mathrm{Re}\left(v_{+1}^T\left(\mathscr{L}_{+1}-\iota\omega\mathbb{I}\right)^{-1}v_{+1}\right) \tag{15}$$

In experiments, usually we are interested in the ratio of P to the applied microwave field B_1. Therefore, $I(\omega)$, the CW absorption signal, is given as:

$$I(\omega) \propto B_1\mathrm{Re}\left(v_{+1}^T\left(\mathscr{L}_{+1}-\iota\omega\mathbb{I}\right)^{-1}v_{+1}\right) \tag{16}$$

in the weak microwave field limit. This is the well-known expression from linear response theory used for calculating unsaturated CW spectra [11, 14, 18].

Similarly, in the Bloch Equation limit, Eq. (9) can be shown [16, 17] to reduce to the well-known equation for CW absorption in the presence of a saturating field B_1:

$$I(\omega) \propto \frac{B_1}{1 + (\omega - \omega_0)^2 T_2^2 + \gamma_e^2 B_1^2 T_1 T_2} \tag{17}$$

Here γ_e is the electron gyromagnetic ratio, B_1 is the applied microwave field, and T_1, T_2 are the longitudinal and transverse electron spin relaxation times, respectively.

In Eq. (3), the spin transition matrix $\mathscr{D}$ relates the off-diagonal coherence orders $p^S = \pm 1$ to $p^S = 0$. Essentially, $\mathscr{D}$ is the contribution of the microwave field to the overall 3 × 3 block stochastic Liouville superoperator that represents the joint evolution of all the coherence orders $p^S = 0, \pm 1$. Given greater values of the microwave field B_1, the various coherences $p^S = \pm 1, 0$ cannot be decoupled from each other.

The block off-diagonal part of the 3 × 3 block matrix in Eq. (3),

$$\begin{bmatrix} 0 & 0 & \imath\mathscr{D} \\ 0 & 0 & -\imath\mathscr{D} \\ \imath\mathscr{D}^T & -\imath\mathscr{D}^T & 0 \end{bmatrix}, \tag{18}$$

is the contribution of the applied microwave field B_1, which is simply obtained from $-i\mathscr{H}_1^{\times}$, where $\mathscr{H}_1 = \gamma_e B_1 S_x$. Here S_x denotes the x-component of the electron spin operator, and $A^{\times}\rho \equiv [A, \rho] = A\rho - \rho A$ denotes the superoperator corresponding to the operator A.

Now, $\imath\mathscr{D}$, in the top right block of Eq. (18), is given by the elements of $\mathscr{H}_1^{\times}$ that propagate from the $p^S = 0$ coherence to the $p^S = +1$ coherence. The elements of $\imath D$ are given as:

$$\begin{aligned} &\left\langle p^S = +1, q^S = 0, \lambda_1 \middle| -\imath\mathscr{H}_1^{\times} \middle| p^S = 0, q^S = \pm 1, \lambda_2 \right\rangle \\ &= \left\langle p^S = +1, q^S = 0, \lambda_1 \middle| -\imath B_1 \mathcal{S}_x^{\times} \middle| p^S = 0, q^S = \pm 1, \lambda_2 \right\rangle \end{aligned} \tag{19}$$

$$= \pm B_1 \imath \frac{1}{2} \delta_{\lambda_1, \lambda_2}. \tag{20}$$

Here λ_1, λ_2 denote the "quantum numbers" that denote the motional degrees of freedom, which stems from the fact that the SLE basis set is a product space of spin and classical motional degrees of freedom. However, $-\imath\mathscr{H}_1^{\times}$ does not affect these motional degrees of freedom, hence the Kronecker δ term $\delta_{\lambda_1, \lambda_2}$ in Eq. (20).

In fact the $\frac{\imath}{2}\delta_{\lambda_1, \lambda_2}$ term in Eq. (20) is exactly the same as the pulse propagator component $\mathscr{P}_{+1 \leftarrow 0}$ that transfers from coherence order $p^S = 0$ to coherence order $p^S = +1$ in a pulsed ESR experiment such as 2D-ELDOR [12], so

$$\imath\mathscr{D} = B_1 \mathscr{P}_{+1 \leftarrow 0} \tag{21}$$

Equation (21) holds for any valid SLE basis, even after basis set symmetrizations [12] such as the M symmetrization and the K symmetrization. Selection rules [11] can also be applied as in the computation of 2D-ELDOR spectra.

By utilizing the fact that the $p^S = -1$ coherence components of the density matrix are complex conjugates of the $p^S = +1$ coherence components, along with the fact that $-\imath\mathscr{K}_1^{\times}$ is complex symmetric, we can populate the remaining block off-diagonal elements of the 3 × 3 block matrix in Eq. (3), namely $-\imath\mathscr{D}$, $\imath\mathscr{D}^T$, and $-\imath\mathscr{D}^T$.

By combining Eqs. (9) and (21), we obtain the following expression for absorbed power in a CW saturation experiment:

$$P \propto \mathrm{Im}\left(\mathbf{Q}^T\mathbf{Z}_{ss}\right) = \mathrm{Im}\left(\begin{bmatrix}\mathbf{Q}\\0\\0\end{bmatrix}^T\begin{bmatrix}\mathscr{L}_{+1}-\imath\omega\mathbb{I} & 0 & \boldsymbol{B}_1\mathscr{P}_{+1\leftarrow 0}\\ 0 & \mathscr{L}_{-1}+\imath\omega\mathbb{I} & -\boldsymbol{B}_1\mathscr{P}_{+1\leftarrow 0}\\ \boldsymbol{B}_1\mathscr{P}^T_{+1\leftarrow 0} & -\boldsymbol{B}_1\mathscr{P}^T_{+1\leftarrow 0} & \mathscr{L}_0\end{bmatrix}^{-1}\begin{bmatrix}\imath\mathbf{Q}\\-\imath\mathbf{Q}\\0\end{bmatrix}\right) \quad (22)$$

Note that the 3 × 3 block matrix in Eq. (22) is still complex symmetric.

Having established a basic framework for calculating the CW saturation spectrum, we now consider the details of the basis set. As in earlier work [12], we utilize the M-symmetrized basis vectors for representing v_{+1}, $\mathscr{L}_0$, $\mathscr{L}_{+1}$, and $\mathscr{L}_{-1}$. Moreover, $\mathscr{L}_{-1}$ and $\mathscr{L}_{+1}$ are complex conjugate transposes of each other, i.e., $\mathscr{L}_{-1} = \mathscr{L}^{\dagger}_{+1}$. In short, all the components of the 3 × 3 block matrix are already available from the 2D-ELDOR theory [12].

3 Results

For evaluating the CW saturation spectrum as in Eq. (9), we use the spsolve solver in Python's Scipy module that solves the resolvent in Eq. (9) for each magnetic field offset value (or equivalently an offset frequency ω after multiplying the field offset $B-B_0$ with the electron gyromagnetic ratio γ_e) by performing a sparse LU decomposition [19] of the sparse 3 × 3 complex symmetric block matrix in Eq. (9). Matrix partitioning is another approach suitable for such computations [20]. While the complex symmetric Lanczos based solvers [21] are an option, they do not work effectively for the case of a saturating microwave field [18]. Moreover, given that most saturation experiments are performed at X band and at motional rates that are not ultraslow, the smaller basis sets are not very large, so using a resolvent based solver is not very time consuming. For cases that involve large SLE matrices [22, 23], one has the option of switching to solvers suitable for sparse matrices such as GMRES [24]. We use a threshold of matrix size 2000 in our fitting routines, above which the program automatically switches from spsolve to gmres. Moreover, we find it advantageous in terms of computational speed to use a diagonal preconditioner [18], given by the following expression based on Eq. (22):

$$M(\omega) = \mathrm{diag}\left(\begin{bmatrix} \mathscr{L}_{+1} - \imath\omega\,\mathbb{1} & 0 & B_1\mathscr{P}_{+1\leftarrow 0} \\ 0 & \mathscr{L}_{-1} + \imath\omega\,\mathbb{1} & -B_1\mathscr{P}_{+1\leftarrow 0} \\ B_1\mathscr{P}^T_{+1\leftarrow 0} & -B_1\mathscr{P}^T_{+1\leftarrow 0} & \mathscr{L}_0 \end{bmatrix}\right). \tag{23}$$

Here diag(A) denotes the diagonal matrix formed by the diagonal entries of a matrix A. Similar preconditioners have been used previously for calculating magnetic resonance spectra [18, 25, 26]. We used a 4 Core 3.20 GHz Windows 10 workstation for our computations. While computational times per spectrum depend on various factors, a typical CW saturation MOMD calculation for 20 orientations and a grid of 128 magnetic field values in Fig. 6 took roughly 200 s.

3.1 Increasing Microwave Field B_1

Equation (17) tells us that the dependence on B_1 is approximately linear for small values of B_1 and decreases as $\propto \frac{1}{B_1}$ for very large values of B_1. The maximum intensity is attained for $B_1 \sim O\left(\frac{1}{\gamma_e\sqrt{T_1T_2}}\right)$.

We show the effect of increasing B_1 on the CW saturation spectrum in Fig. 1

As expected, the central peak first increases in height, then decreases when B_1 is large. There are empirical relations [4, 5] for the central peak–peak amplitude as a function of B_1. While we strongly recommend using our simulation and fitting routines given their rigorous grounding in stochastic Liouville theory, we demonstrate here for the sake of completeness the fit of the central peak-peak amplitude calculated by our SLE simulations in Fig. 2 to the following empirical relation:

$$I(B_1) = \frac{I_0 B_1}{\left(1 + PB_1^2\right)^{\epsilon}} \tag{24}$$

Here I_0 is a proportionality constant, P is the saturation parameter $P = \gamma_e^2 T_1 T_2^{eff}$, and ϵ is an empirical correction factor. Typically $\epsilon \sim 1.5$ for homogeneous broadening and $\epsilon \sim 0.5$ for inhomogeneous broadening.

We use MATLAB's cftool to perform this least squares fit using the *trust region* algorithm. We used the following settings in cftool:

- Lower/upper bounds for I_0: $[0, \infty)$
- Lower/upper bounds for P: $[0, \infty)$
- Lower/upper bounds for ϵ: $[0, \infty)$
- tolFun: 10^{-6}
- tolX: 10^{-6}

The R^2 value of the fit was 0.9994. Here are the fit parameters along with their 95% confidence intervals (Table 1):

The fit value of $\epsilon = 1.582$ is close to 1.5, which is appropriate because the simulated spectra are homogeneously broadened and no additional inhomogeneous broadening was included.

3.2 Effect of Motional Rate

The effect of motional rate is similar to the effect of motional rate on unsaturated CW spectra—at motional rates approaching $10^9 s^{-1}$ at X band, we see three sharp hyperfine lines. As the motional rate slows down, we see that the lines get broader. In the motional narrowing region where the diffusion tensor $R \gtrsim 10^9 s^{-1}$ at X-band, we see that the effects of saturation are visible merely as an increased linewidth and decreased intensity in the sharp hyperfine lines.

Figure 3 shows the dependence of CW saturation spectra on the motional rate. While our formulation supports non-isotropic diffusion tensors and arbitrary diffusion and magnetic frame tilt angles, we chose an isotropic diffusion tensor for simplicity.

3.3 Effect of Heisenberg Exchange ω_{ss}

Heisenberg exchange leads to both an overall broadening of the CW saturation spectra, and transfer of saturation among the hyperfine components. Saturation spectra can be used to measure Heisenberg exchange rates in order to determine the accessibility of side chains such as in T4 Lysosyme [5]. In Fig. 4, we show the effect of Heisenberg exchange on a nitroxide spectrum.

4 Least Squares Fitting Package

A key advantage of our general SLE-based approach is that we can perform non-linear least-squares fitting [13] of CW saturation spectra to fit motional and other parameters in a rigorous manner, requiring fewer experimental measurements of CW saturation spectra. To perform automated least-squares fitting, we employ a current version the Levenberg Marquardt algorithm available under the scipy. optimize and lmfit packages in Python. With the advent of robust and powerful scientific computing libraries, we can connect our software for computing CW saturation spectra to such packages that support state-of-the-art features such as constrained optimization, automatically generated goodness-of-fit reports such as χ square, information criteria [27], etc. Given the parameters listed in Table 2 that can have an effect on the CW saturation spectrum, these libraries make it much easier for the experimentalist to quickly explore various fit parameters and understand their uncertainties in an automated fashion. Typically we set $R_{xx} = R_{yy} = R_\perp$ and $R_{zz} = R_\parallel$. To avoid correlation problems sometimes we fit $R_\parallel$ and $R_\perp$ and other times we fit $\bar{R} \equiv \sqrt{R_\parallel R_\perp^2}$ and $N \equiv \frac{R_\parallel}{R_\perp}$.

Given the virtues of using these advanced fitting packages readily available open-source in Python and specifically in lmfit, we have chosen to proceed with lmfit as our primary non-linear least-squares fitting routine. lmfit also provides options for utlizing other advanced

fitting routines such as Markov chain Monte Carlo [28, 29] and Nelder-Mead simplex [28, 29] that provide additional tools for performing challenging non-linear least square fits.

To illustrate the utility of lmfit, we perform the following non-linear least-squares fit to a model spectrum and show the results in Fig. 5. We generated a CW spectrum and then randomly initialize F, R_{xx}, R_{yy}, and R_{zz}, allowing the other parameters to stay at their actual model values. With initial parameter settings for R_{xx}, R_{yy}, R_{zz}, F to be far from their actual values, we test how long it takes for lmfit to converge to the actual values of R_{xx}, R_{yy}, R_{zz}, F. In Fig. 5 one sees how the CW saturation spectrum corresponding to the initial seed parameters predicts a completely different spectrum (shown in orange on the left subplot), whereas after fitting, the predicted and model spectrum (shown in blue in both subplots) agree very well. In addition, the best fit parameters occur *exactly* at their actual values in 97 function evaluations. By adding noise to the model spectrum, we might reduce the quality of fit slightly, but we still expect our approach to yield robust fits. Note that we let $R_{xx} = R_{yy}$ as is typically done. A wise heuristic would be to add such constraints such as this one, and then relax them when one is close to the best fit, in order to achieve further fine tuning. lmfit is an excellent package for specifying such arbitrary constraints.

Here are the results of the least squares fit reported by lmfit:

- Fitting method: Levenberg Marquardt least squares
- Number of function evaluations: 97
- Data points in the spectrum: 256
- Number of independent fit parameters: 3
- χ square: 3.8364×10^{-30}
- Akaike information criterion: [27]—18753.22
- Bayesian information criterion: [27]—18742.58

Here are the best fit values of the parameters:

5 Least Squares Fitting of Slow-Motional Lipid Saturation Spectra

As described in Sect. 4, we can fit experimental CW saturation spectra. We performed least squares fits to experimental spectra from randomly ordered (MOMD) 5PC-DMPC lipid spectra [4] at $39°C$ showing our theoretical and numerical fitting approach when combined with the MOMD model [11]. As noted in Sect. 3, Lanczos type solvers are not recommended for computing CW saturation spectra. But one can first use the nlsl package [13] to fit unsaturated CW spectra when the microwave field B_1 is low enough. This would yield an initial set of parameters. Then one could optimize them by fitting the set of saturated and unsaturated spectra. We followed this approach for our fits shown in Fig. 6. Given the decay in peak-peak amplitudes for large values of B_1 as seen in Fig. 2, performing simultaneous fitting of multiple saturation spectra can lead to excessive weight towards spectra with high peak–peak amplitudes. Therefore we chose a simple reweighting strategy for our simultaneous fits to CW saturation spectra corresponding to multiple values

of B_1. For the purposes of least squares fitting, we reweigh each derivative CW saturation spectrum by the following factor:

$$W_k = \frac{1}{\max_\omega X_{k,\text{expt}}(\omega) - \min_\omega X_{k,\text{expt}}(\omega)}, \tag{25}$$

where $X_{k,\text{expt}}(\omega)$ denotes the experimental derivative CW spectrum at frequency ω, corresponding to the kth value of the microwave field B_1 in the set of experimental CW saturation spectra being simultaneously fit.

The overall least squares residual to be minimized, thus becomes the following:

$$C = \sum_{k=1}^{N} \sum_{\omega} \left(W_k \times \left(X_{k,\text{expt}}(\omega) - X_{k,\text{sim}}(\omega)\right)\right)^2, \tag{26}$$

where $k \in \{1, 2, \ldots N\}$ denote the set of experimental CW saturation spectra being simultaneously fit. Each k nominally corresponds to a different value of B_1.

Just like $X_{k,expt}(\omega)$, $X_{k,sim}(\omega)$ denotes the simulated derivative CW spectrum corresponding to the kth value of B_1 in the set of experimental spectra being simultaneously fit. While we chose a simple form of the least-squares residual in Eq. (26), lmfit provides options for creating custom residual functions.

The fit parameters are given in the following table:

The g and A tensor parameters were assumed to be as follows, partially based on previous work: [30, 31].

6 Conclusion

In this work, we showed the correspondence between the theory of 2D-ELDOR and the theory of CW saturation spectra, thereby creating a rigorous paradigm for simulating and fitting CW saturation spectra that includes all the dynamical parameters that are relevant to many studies involving CW saturation ESR, and connect our approach with state-of-the-art fitting packages in Python. This approach is then applied to analyze an experimental case. We shall release our software as a Python package for the benefit of the ESR community. Our SLE-based approach to saturation is quite general and can be applied to other saturation-based ESR methods such as pulsed saturation recovery [32]. An additional advantage of our approach is that it provides an extra “dimension” as one simultaneously fits spectra as a function of microwave field B_1, since this provides more independent data to extract the parameters to be fit.

Acknowledgements

This work is supported by Grant no. P41GM103521 (NIGMS/NIH) from the National Institute of General Medical Sciences (NIGMS). We also wish to acknowledge the comments of Siddarth Chandrasekaran and Alex Lai.

Data Availability Statement

The data and computer programs that support the findings of this study are available from the corresponding author upon reasonable request.

References

1. Borbat PP, Mchaourab HS, Freed J, J. Am. Chem. Soc 124, 5304 (2002) [PubMed: 11996571]
2. Jeschke G, Ann. Rev. Phys. Chem 63, 419 (2012) [PubMed: 22404592]
3. Knowles PF, Marsh D, Biochem. J 274, 625 (1991) [PubMed: 1849401]
4. Dzikovski B, Livshits V, Freed JH, J. Phys. Chem. B 119, 13330 (2015) [PubMed: 26490692]
5. Altenbach C, Froncisz W, Hemker R, Mchaourab H, Hubbell WL, Biophys. J 89, 2103 (2005) [PubMed: 15994891]
6. Snead D, Lai AL, Wragg RT, Parisotto D, Ramdall T, Dittman J, Freed JH, Eliezer D, Front. Mol. Neurosci 10, 154 (2017) [PubMed: 28596722]
7. Meirovitch E, Nayeem A, Freed JH, J. Phys. Chem 88, 3454 (1984)
8. Stephen MJ, Fraenkel GK, J. Chem. Phys 32, 1435 (1960)
9. Freed JH, J. Chem. Phys 43, 2312 (1965)
10. Goldman SA, Bruno GV, Freed JH, J. Chem. Phys 59, 3071 (1973)
11. Meirovitch E, Igner D, Igner E, Moro G, Freed JH, J. Phys. Chem 77, 3915 (1982)
12. Lee S, Budil D, Freed JH, J. Chem. Phys 101, 5529 (1994)
13. Budil D, Lee S, Saxena S, Freed JH, J. Magn. Reson. A 120, 155 (1996)
14. Freed JH, Bruno GV, Polnaszek C, J. Chem. Phys 55, 5270 (1971)
15. Freed JH, Bruno GV, Polnaszek CF, J. Phys. Chem 75(22), 3385 (1971)
16. Freed JH, J. Phys. Chem 78(12), 1155 (1974)
17. Freed JH, in Time Domain Electron Spin Resonance, Chap. 2, ed. by Kevan L, Schwartz RN. Theory of ESR Saturation Recovery in Liquids and Related Media, (Wiley, 1979), p. 31
18. Schneider D, Freed JH, in Lasers, Molecules and Methods, Chap. 10, ed. by Hirschfelder, Wyatt, Coalson. Spin Relaxation and Motional Dynamics, (McGraw-Hill, 1989), p. 431
19. Davis TA, ACM Trans. Math. Softw 30, 196 (2004)
20. Bruno G, Application of the Stochastic Liouville Method in Calculating ESR Lineshapes in the Slow Tumbling Region and an ESR-ELDOR Study of Exchange, PhD Dissertation, Cornell University, Department of Chemistry and Chemical Biology (1973)
21. Moro G, Freed JH, J. Chem. Phys 75, 3157 (1981)
22. Kuprov I, J. Magn. Reson 208, 179 (2011) [PubMed: 21169043]
23. Gupta P, Liang Z, Freed JH, J. Chem. Phys 152, 214112 (2020) [PubMed: 32505151]
24. “Scipy v1.6.2 reference guide”. https://docs.scipy.org/doc/scipy/reference/generated/scipy.sparse.linalg.gmres.html. Accessed 20 Apr 2021
25. Schneider D, in Spectral decompositions and slow motional lineshape analysis. In: Rocky mountain conference on analytical chemistry (2004)
26. Kuprov I, J. Magn. Reson 270, 124 (2016) [PubMed: 27470597]
27. Konishi S, Kitagawa G, Information Criteria and Statistical Modeling (Springer, Berlin, 2008)
28. Newville M, Stensitzki T, Allen DB, Rawlik M, Ingargiola A, Nelson A, in Lmfit: Non-Linear Least-Square Minimization and Curve-Fitting for Python. Astrophysics Source Code Library, record ascl:1606.014 (2016)
29. Stoll S, Schweiger A, J. Magn. Reson 178(1), 42 (2006) [PubMed: 16188474]
30. Gaffney BJ, McConnell HM, J. Mag. Res 16, 1 (1974)
31. Dzikovski B, Tipikin D, Freed JH, J. Phys. Chem. B 116, 6694 (2012) [PubMed: 22324811]
32. Eaton SS, Eaton GR, in Biological Magnetic Resonance 24/B, Chap. 1, ed. by Eaton SS, Eaton GR, Berliner L. Saturation Recovery EPR, (Springer, 2005)

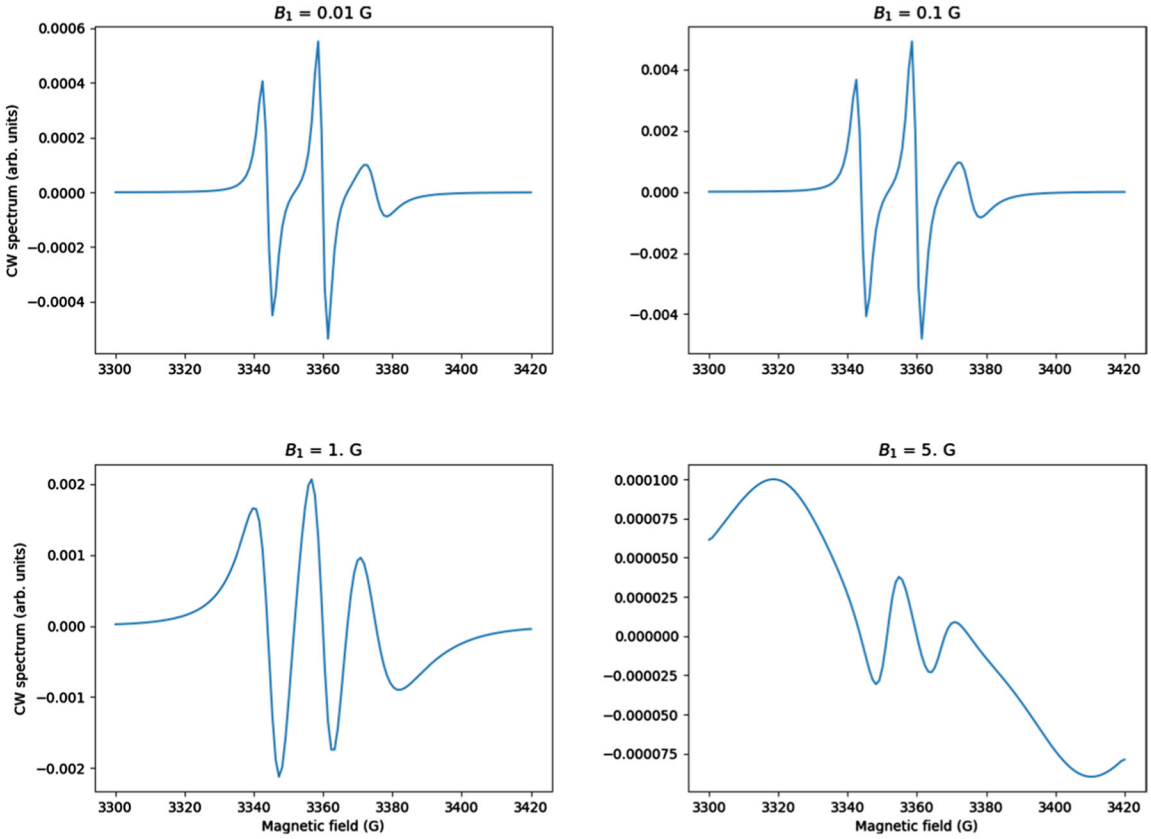

Fig. 1.

CW saturation spectra as a function of B_1. $g_{xx} = 2.0087$, $g_{yy} = 2.0057$, $g_{zz} = 2.0021$, $A_{xx} = A_{yy} = 6$ G, $A_{zz} = 36$ G. Motional rate $R_{xx} = R_{yy} = R_{zz} = 10^8\ s^{-1}$, electronic longitudinal spin relaxation rate $W_e = \frac{1}{2T_1} = 10^5 s^{-1}$. Static field $B_0 = 3360$ G (X band)

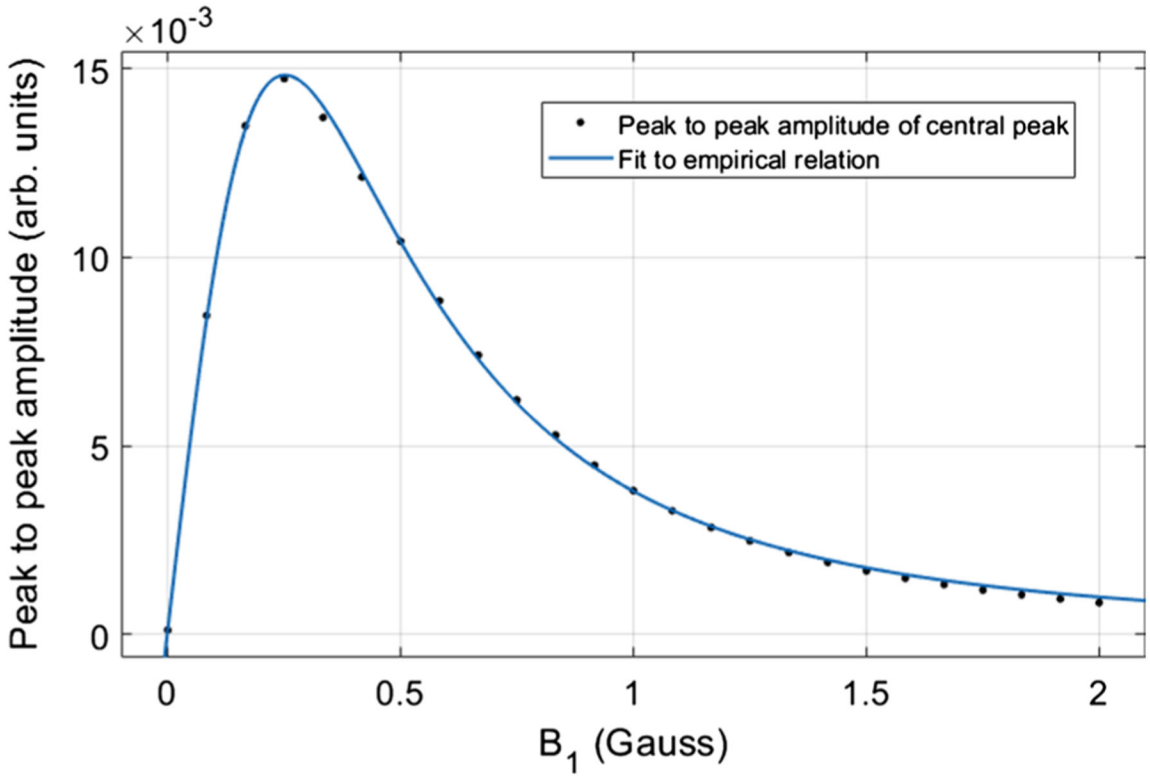

Fig. 2.

Central peak-peak amplitude for CW saturation spectra as a function of B_1. $g_{xx} = 2.0087$, $g_{yy} = 2.0057$, $g_{zz} = 2.0021$, $A_{xx} = A_{yy} = 6$ G, $A_{zz} = 36$ G. Motional rate $R_{xx} = R_{yy} = R_{zz} = 10^8\ s^{-1}$, $W_e = 10^5\ s^{-1}$. Static field $B_0 = 3360$ G (X band)

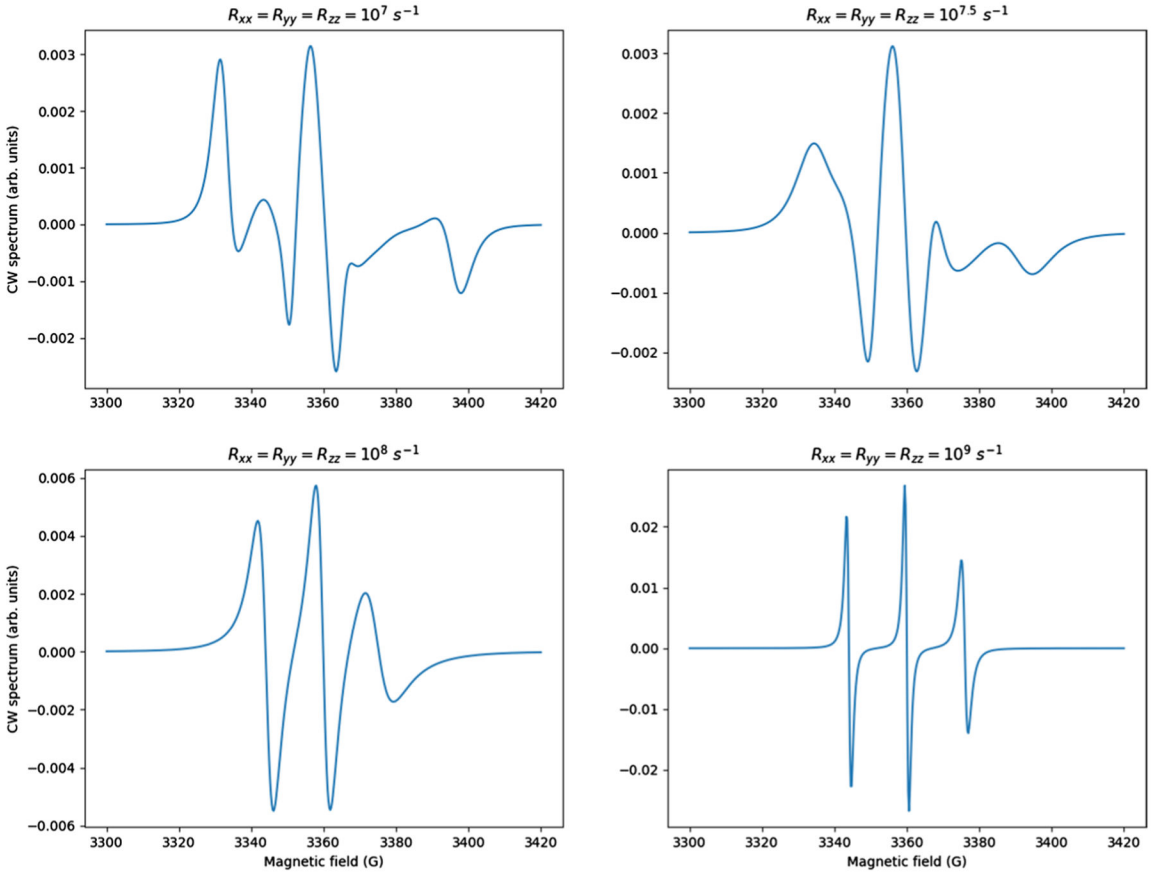

Fig. 3.

CW saturation spectra as a function of the rotational diffusion rate. $g_{xx} = 2.0087$, $g_{yy} = 2.0057$, $g_{zz} = 2.0021$, $A_{xx} = A_{yy} = 6$ G, $A_{zz} = 36$ G. $W_e = 10^5\ s^{-1}$. Static field $B_0 = 3360$ G (X band). $B_1 = 0.5$ G

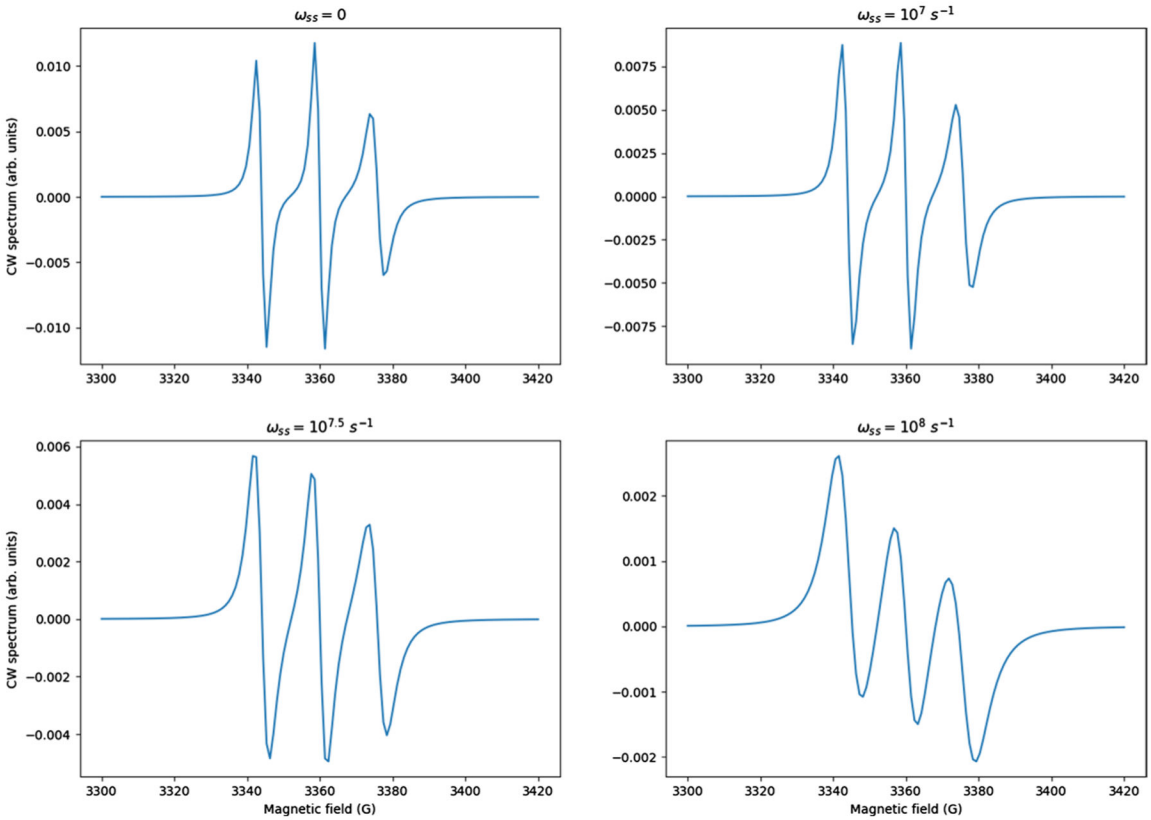

Fig. 4.

CW saturation spectra as a function of the Heisenberg exchange rate, ω_{ss}. We use a motional rate of $R_{xx} = R_{yy} = R_{zz} = 3.1623 \times 10^8\ s^{-1}$ $g_{xx} = 2.0087$, $g_{yy} = 2.0057$, $g_{zz} = 2.0021$, $A_{xx} = A_{yy} = 6$ G, $A_{zz} = 36$ G. Longitudinal spin relaxation rate $W_e = 10^5\ s^{-1}$. Static field $B_0 =$ 3360 G (X band). $B_1 = 0.5$ G

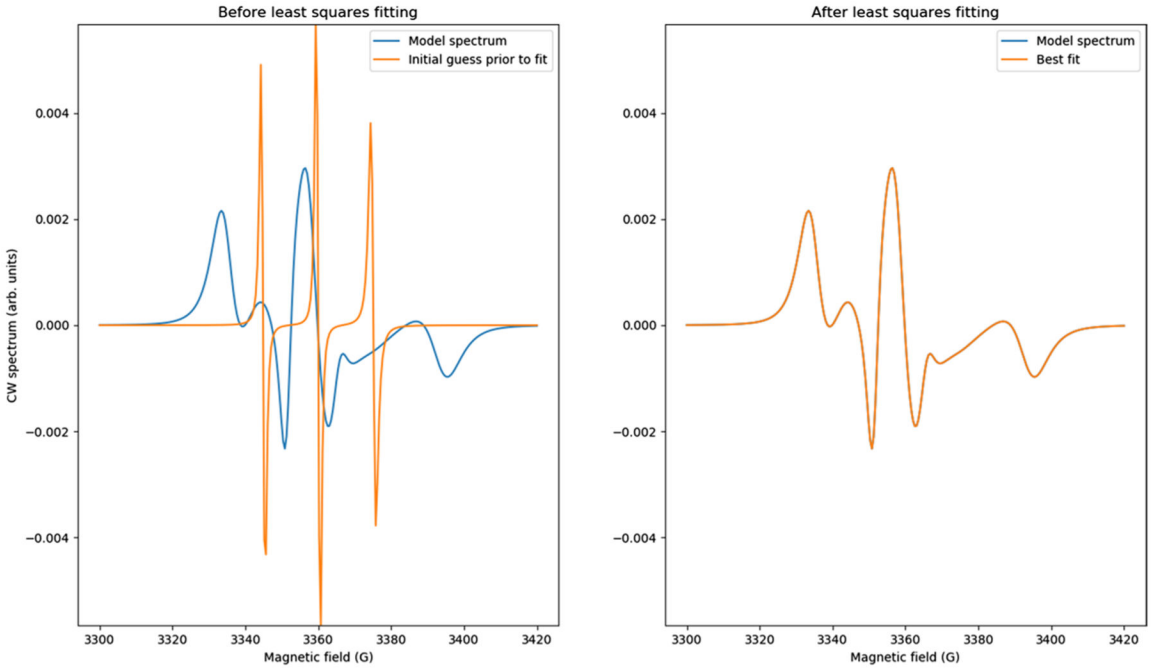

Fig. 5.

Non-linear least squares fit to CW saturation spectra. The model spectrum has a motional rate of $R_{xx} = R_{yy} = 1.51 \times 107\ s^{-1}$, $R_{zz} = 108\ s^{-1}$, $g_{xx} = 2.00882$, $g_{yy} = 2.0062$, $g_{zz} = 2.00233$, $A_{xx} = 5.2$ G, $A_{yy} = 5.8$ G, $A_{zz} = 34.4$ G. The scale parameter F is chosen to be 1.0, and $B_1 = 0.5$ G. We used the lmfit package in Python and allowed the scale parameter F, the x and y diffusion rates R_{xx}, R_{yy} with the constraint $R_{xx} = R_{yy} = R_{\perp}$, and the z diffusion rate $R_{zz} = R_{\parallel}$ to vary. Here $W_e = 8.8 \times 10^4\ s^{-1}$. Static field $B_0 = 3360$ G (X band). Results of the fit are summarized in Table 3

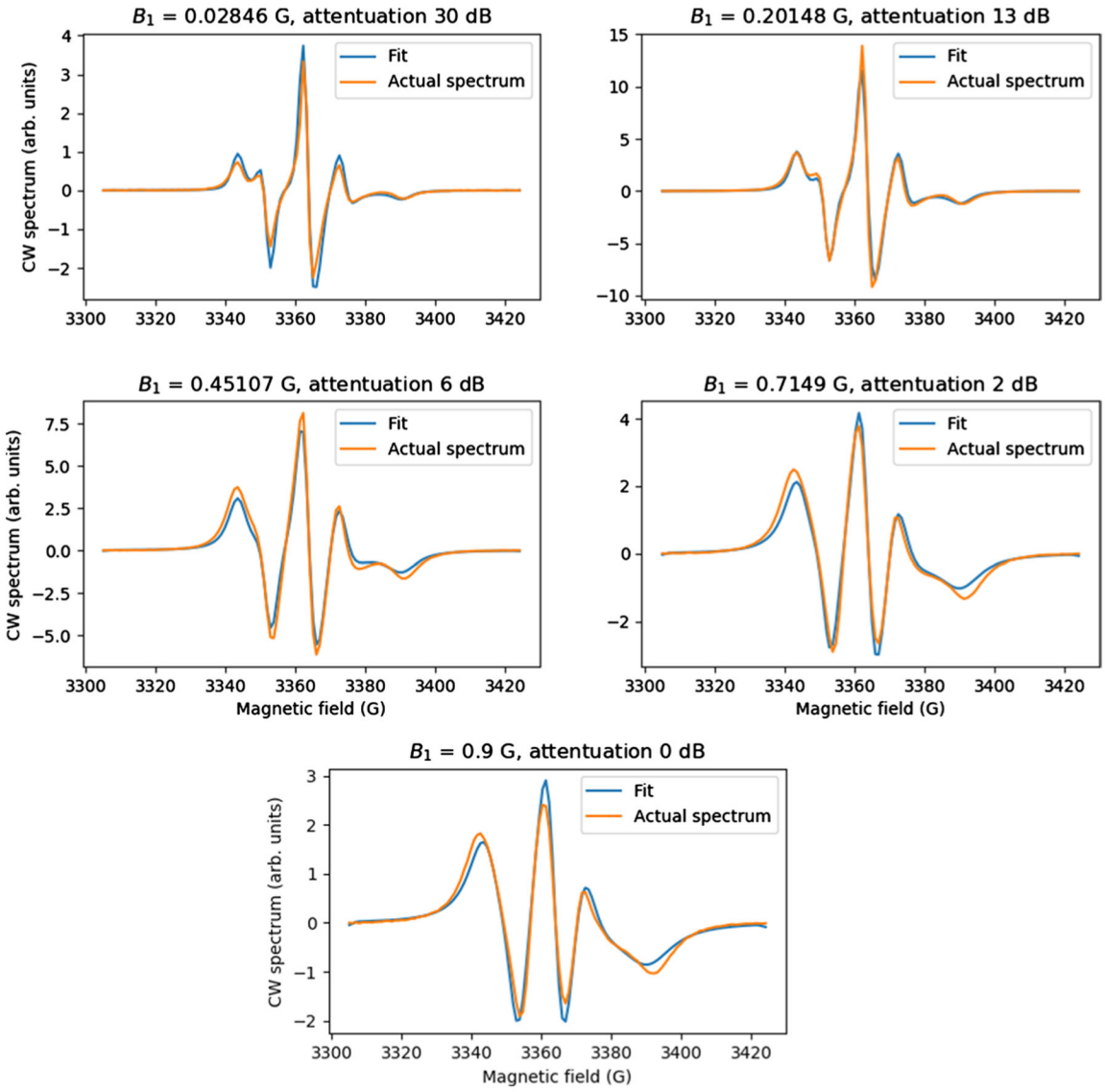

Fig. 6.

Fit to experimental 5PC-DMPC CW saturation spectra at 39°*C*. The fit parameters are listed in Table 4. Static field B_0 = 3360 G (X band). The maximum value of B_1 determined for a small sample of PADS, as described by Goldman Bruno, and Freed [10], was 0.97 Gauss. With the correction for the difference in resonator *Q*-values, this number for the 5PC-in-DMPC sample was estimated as 0.9 Gauss. We used 20 orientations per MOMD calculation. χ^2 residual for the simultaneous fits was 0.57 [28] (Table 5).

Table 1

Non-linear least squares fit parameters for Fig. 2

Parameter	Fit value	95% confidence interval
I_0	0.1073	(0.1052, 0.1093)
P	7.263 G^{-2}	(6.875, 7.65) G^{-2}
ϵ	1.582	(1.549, 1.615)

Table 2

List of model parameters used for fitting/simulating CW saturation spectra

Parameter name	Parameter symbol	Description
g_{xx}, g_{yy}, g_{zz}	gxx, gyy, gzz	g tensor
A_{xx}, A_{yy}, A_{zz}	axx, ayy, azz	A (hyperfine) tensor (G)
α_D, β_D, γ_D	ald, bed, gad	Diffusion tilt angles (°)
α_m, β_m, γ_m	alm, bem, gam	Magnetic tilt angles (°)
ψ	psi	Director tilt (°)
$\left\{c_K^L\right\}$	c20, c22, c40, c42, c44	Coefficients for orienting potential
B_0	b0	Static field (G)
B_1	b1	Saturating microwave field (G)
R_{xx}, R_{yy}, R_{zz}	dx, dy, dz	Log_{10} of rotational diffusion tensor (s^{-1})
ω_{ss}	oss	Log_{10} of Heisenberg spin exchange rate (s^{-1})
$2I$	in2	Twice the nuclear spin, I
L_{emx}, L_{omx}, K_{mx}, M_{mx}, P_{mx}^I	lemx, lomx, kmx, mmx, ipnmx	Basis set truncation indices
n_{MOMD}	nort	Number of orientations in MOMD model
$\left(T_{2e}^{-1}\right)^{(0)}$, $\left(T_{2e}^{-1}\right)^{(2)}$	t2edi, t2efi	Log_{10} of angular dependent homogeneous T_{2e}^{-1} tensor (s^{-1})
$2W_e$	t1edi	Log_{10} of longitudinal electron spin-relaxation rate (s^{-1})
$2W_n$	t1ndi	Log_{10} of additional longitudinal nuclear spin-relaxation rate (s^{-1})
F	scale	Overall scale factor that multiplies the entire spectrum by a constant factor for the purposes of fitting
X_{shift}	shiftg	Shifts the entire spectrum laterally for the purposes of fitting
Δ_G	gib0	Gaussian inhomogeneous broadening (peak–peak width, Gauss)
$\Delta_G^{(2)}$	gib2	Director-frame-dependent Gaussian inhomogeneous broadening (p–p width, Gauss)

Table 3

Best fit values reported by lmfit corresponding to Fig. 5

Parameter symbol	Parameter name	Fit value	Initial guess value
dx	$\log_{10}(R_{xx})$	7.2	9.5
dy	$\log_{10}(R_{yy})$	7.2 [dy constrained to be equal to dx]	9.5
dz	$\log_{10}(R_{zz})$	8.0	9.5
scale	F	1.0	0.1

Table 4

Fit values corresponding to Fig. 6

Parameter symbol	Parameter name	Fit value
dx	$\log_{10}(R_{xx}$ in $s^{-1})$	8.18
dy	$\log_{10}(R_{yy}$ in $s^{-1})$	8.18
dz	$\log_{10}(R_{zz}$ in $s^{-1})$	9.27
scale	F	1866.29
c20	c_0^2	2.0
t1edi	$\log_{10}(2W_e)$	5.046
gib0	Δ_G	1.94 Gauss

Table 5

g and *A* tensor values for 5PC-in-DMPC

Parameter symbol	Parameter name	Value
gxx	g_{xx}	2.00882
gyy	g_{yy}	2.0062
gzz	g_{zz}	2.00233
axx	A_{xx}	5.2 Gauss
ayy	A_{yy}	5.8 Gauss
azz	A_{zz}	33.5 Gauss